

This document is the unedited Author's version of a Submitted Work that was subsequently accepted for publication in **ACS Applied Nano Materials**, copyright © American Chemical Society after peer review.

To access the final edited and published work see
<https://pubs.acs.org/doi/10.1021/acsanm.0c02553>.

Atomic Layer Deposition of MoSe₂ Nanosheets on TiO₂ Nanotube Arrays for Photocatalytic Dye Degradation and Electrocatalytic Hydrogen Evolution

Raul Zazpe,^{1,2} Richard Krumpolec,³ Hanna Sopha,^{1,2} Jhonatan Rodriguez-Pereira,¹ Jaroslav Charvot,⁴ Luděk Hromádka,^{1,2} Eva Kolíbalová,² Jan Michalička,² David Pavlíňák,³ Martin Motola,¹ Jan Přikryl,¹ Miloš Krbal,¹ Filip Bureš,⁴ and Jan M. Macak,^{1,2}*

¹Center of Materials and Nanotechnologies, Faculty of Chemical Technology, University of Pardubice, Nam. Cs. Legii 565, 530 02 Pardubice, Czech Republic.

²Central European Institute of Technology, Brno University of Technology, Purkynova 123, 612 00 Brno, Czech Republic.

³Department of Physical Electronics, CEPLANT - R & D Center for Plasma and Nanotechnology Surface Modifications, Faculty of Science, Masaryk University, Kotlářská 267/2, 611 37 Brno, Czech Republic.

⁴Institute of Organic Chemistry and Technology, Faculty of Chemical Technology, University of Pardubice, Studentská 573, 532 10, Pardubice, Czech Republic.

Keywords: MoSe₂, nanosheets, atomic layer deposition, TiO₂ nanotube layers, catalysis

Abstract

Herein, hierarchical MoSe₂/1D TiO₂ nanotube layer structure was successfully fabricated in a simple and fast fashion and its photocatalytic and electrocatalytic properties were assessed. The novelty of this work lies in the utilization of Atomic Layer Deposition (ALD) technique to deposit MoSe₂ nanosheets on 1D TiO₂ nanotube layers. The photoelectrochemical and photo- and electrocatalytic properties were explored and optimized as a function of the MoSe₂ALD cycles. ALD allowed precise control on MoSe₂ nanosheet size, and in turn, on the surface structure, which is pivotal for efficient catalysts. The MoSe₂ nanosheets grew on both inner and outer 1D TiO₂ nanotube surface mainly perpendicularly oriented, maximizing the exposed active edges, an essential aspect to fully exploit the MoSe₂ photo- and electrochemical properties. Outstanding photo- and electrocatalytic activity were recorded in both dye organic pollutant degradation and hydrogen evolution reaction applications, respectively. The excellent photocatalytic and electrochemical activity stems from the synergy between tailored ALD loading of MoSe₂ nanosheets on 1D TiO₂ nanotubular structure with high surface/volume ratio, which provided fast electron transfer and easy access to the MoSe₂ active edges, boosting the catalytic activity.

1. Introduction

Heterogeneous catalysis is pivotal process in a great number of industrial chemical technologies, environmental remediations, and also for renewable energy sources, such as fuel cells or hydrogen energy.¹⁻⁴ The importance of heterogenous catalysis continuously increases and correspondingly

also the demand for efficient catalysts increases. Recently, two-dimensional (2D) transition metal dichalcogenides (TMDs) have emerged as suitable catalysts with enhanced selectivity, activity and stability as a result from the intense researching efforts devoted for the development of alternative 2D materials to graphene.⁵ The main driving force behind those efforts are the unparalleled electronic, optical and structural properties that the 2D materials offer in comparison with their bulk counterparts, which provide new possibilities in a wide number of applications ranging from optoelectronics and nanoelectronics to sensing and catalysis.⁶⁻¹¹ 2D TMDs are very promising materials for catalytic applications, essentially due to their extremely enhanced surface-to-volume ratio and the capability of tuning their catalytically active edge sites.^{12,13} Furthermore, they represent affordable and promising alternative catalytic earth-abundant materials to replace the high cost and low abundance Pt group metals.^{14,15} 2D TMDs, with the composition MX_2 (M = Mo or W; X = S, Se, or Te), have layered structure, where a single layer is comprised of transition metal atoms sheet sandwiched between two sheets of chalcogen atoms. The intralayer M-X bonds are covalent, while the layers interact by weak van der Waals forces leading to a graphene-like layered structure.⁵ Among the 2D TMDs family, 2D MoSe_2 has recently attracted growing interest due to its intriguing properties.¹⁶ MoSe_2 exhibits two main phases, namely semiconducting 2H phase with trigonal prismatic coordination and metallic 1T distorted octahedral phase. Despite metallic properties would be highly desirable for enhancing charge transfer resistance, the metallic 1T phase is metastable and easily converts to the stable 2H phase.¹⁷ The inherent metallic nature of Se, offering higher electrical conductivity than that of MoS_2 , has driven recently several works focused on MoSe_2 performance into electrochemical applications such as supercapacitors.^{18,19} Similarly, the graphene-like layered structure with an interlayer spacing (0.646 nm), larger than that of graphene (0.335 nm) and MoS_2 (0.615 nm), is convenient towards reversible insertion of

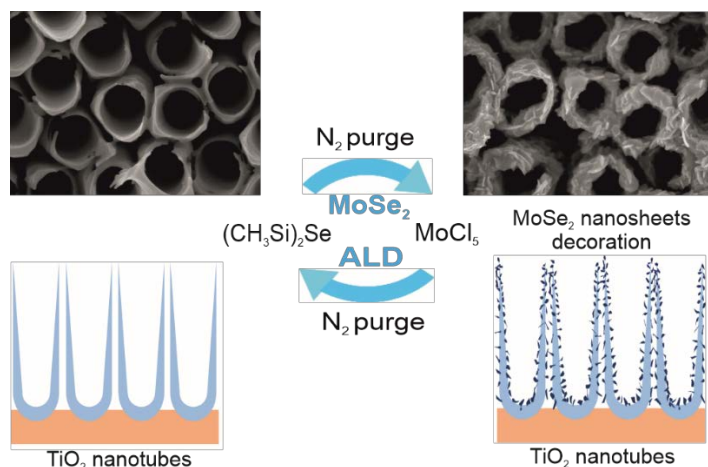
electrolyte ions in energy storage applications as alternative electrode in lithium ion and sodium ion batteries.^{20–22} Likewise, higher optical absorbance and faster photoresponse (than that of MoS₂), have triggered strong interest in the introduction of MoSe₂ into optoelectronic applications.^{23–25} In parallel, its narrow bandgap (1.33–1.72 eV), low cost, high resistance to photocorrosion, large active surface area, and electrochemically active unsaturated Se edges have been exploited by other works, which have studied the nanostructured MoSe₂ performance as sensor and photocatalyst.^{26–29} More importantly, lower Gibbs free energy (close to zero) on MoSe₂ edges for hydrogen adsorption results in higher H coverage as compared with MoS₂, stimulating the study of MoSe₂ as alternative catalytic material for hydrogen evolution reaction (HER). In that direction, different works have reported exfoliation and solvothermal techniques for the deposition of 1T phase and exploitation in HER.^{30–32}

However, MoSe₂ catalytic performance is constrained due to inactive basal planes (active sites only exist at the edges states), low light absorption efficiency, slow charge transfer of the intrinsic semiconducting 2H-phase, along with (as any semiconductor) recombination issues of the photogenerated electron–hole pairs. Those intrinsic limitations are addressed on the one hand by the fabrication of hybrid nanostructures using supporting materials for enhancing electron transfer and charge carrier recombination rate. Diverse substrates have been utilized to host MoSe₂ and improve the electrocatalytic properties, including carbon nanotubes,³³ carbon nanofibers,³⁴ graphene,^{35,36} fluorine doped tin oxide,³⁷ perovskites,³⁸ SnO₂ nanotubes,³⁹ core–shell MoO₂/MoSe₂ nanostructures,⁴⁰ TiO₂ nanotubes and nanoparticles.^{41,42} On the other hand, as the electrocatalytic activity is mainly ascribed to unsaturated Se edge atoms, the growth of vertically oriented few-layer MoSe₂ nanosheets, maximizing the number of exposed Se edges and facilitating

ion/electrolyte transport through, would drive to a great enhancement of the MoSe₂ catalytic performance.⁴³

To date, different methods have been reported for the synthesis of nanostructured MoSe₂ such as, hydrothermal,^{20–22,28,29,35,37,42,44–48} solvothermal,^{33,34,39} liquid exfoliation,^{26,49} electrodeposition,^{19,41} hot filament vapor chemical deposition,⁵⁰ chemical vapor deposition,^{23–25,51} electrochemical atomic layer deposition,⁵² and atomic layer deposition.^{53–55} Most methods reported successful MoSe₂ synthesis, yet also display diverse limitations in controlling key parameters, such as the morphology, the composition and the homogeneity of the synthesized MoSe₂. In contrast, atomic layer deposition (ALD) is a well-established bottom-up deposition technique based on alternating gas-surface self-limited reactions using vapor-phase precursors that offers an unparalleled control over the thickness and the composition of the materials deposited.⁵⁶ ALD has proven by far to be the most suitable technique of choice for depositing materials in uniform and conformal fashion over complex and large area substrates.^{57,58} A newly review summarized the recent progress on ALD and confirmed the suitability of such technique towards the synthesis of different 2D layered materials.⁵⁹

In this work, we further expand our previous works based on 1D TiO₂ nanotube layers (TiO₂ NTs) combined with MoSe_xO_y and MoS₂ deposited by ALD in order to assess the photoelectrochemical, photocatalytic properties and the potential as anode for Li-ion microbatteries.^{60–62} Herein, we evaluated and exploited for the first time the combination of MoSe₂ nanosheets deposited by ALD on 1D TiO₂ NTs and their photo- and electrocatalytic properties by a rationally designed hierarchical structure ALD MoSe₂/1D TiO₂ NTs fabricated in a simple and fast fashion as illustrated in Scheme 1.



Scheme 1. SEM top view and schematic illustration of anodic TiO₂ NTs (left) before being deposited by MoSe₂ ALD process (center) for fabricating MoSe₂/TiO₂ nanotubular heterostructure (right).

The ALD MoSe₂ was deposited using MoCl₅ as Mo precursor and Bis(trimethylsilyl)selenide – (Me₃Si)₂Se, whose feasibility as Se precursor was reported in our recent works.^{53,54} TiO₂ NTs, characterized by the semiconducting nature of TiO₂, unique tubular architecture, chemical stability and large active surface area, are ideal supporting platform for the deposition of MoSe₂. Hence, promising synergistic properties can be expected and exploited for a number of applications. Thus, we explored and evaluated both electrochemical and photocatalytic properties of the ALD MoSe₂/TiO₂ composite nanotubular structure assessed through hydrogen evolution reaction and dye organic pollutant degradation applications, respectively. The high-performance results confirm the synergistic properties stemming from the composite nanotubular structure and numerous catalytically active edge sites of MoSe₂.

2. Experimental methods

The self-organized TiO₂ NTs were fabricated via electrochemical anodization of Ti foils. Prior to all anodizations, Ti foils were degreased by sonication in *isopropanol*, acetone, *isopropanol* and dried by a nitrogen jet, respectively. To obtain ~5 μm thick TNTs (2.25 cm² macroscopic area)

with a diameter of ~230 nm, anodization of Ti foils (Sigma-Aldrich, 0.127 mm thick, 99.7 % purity) was conducted as previously reported.⁶³ Briefly, clean Ti foils were anodized at 18 °C using a high-voltage potentiostat (PGU-200V, Elektroniklabor GmbH) in ethylene glycol based electrolyte containing 10 % water and 0.15 M NH₄F at 100 V for 4 h in a two-electrode configuration using Ti foil as a working electrode and Pt foil as a counter electrode. After anodization, the TiO₂ NTs were sonicated in *isopropanol* and dried in air. The as-prepared amorphous TiO₂ NTs turned into anatase phase upon post-annealing process in a muffle oven at 400 °C for 1 h.⁶⁴

The deposition of MoSe₂ on annealed TiO₂ NTs was carried out in a custom-made thermal ALD system at chamber pressure 2 mbar applying a deposition temperature of 300 °C. The Mo precursor, MoCl₅ (Strem, anhydrous 99.6%), and synthesized Bis(trimethylsilyl)selenide – (Me₃Si)₂Se were heated up to get sufficiently high vapor pressure at 120 and 55 °C, respectively. The ALD process was initiated immediately after 5 pulses of ultrapure water were applied to increase the number of hydroxyl active sites on the substrates surface. The ALD parameters applied were as follows: Se precursor (400 ms) – N₂ purge (5 s) – Mo precursor (400 ms) – N₂ purge (5 s). The number of cycles applied were 5, 20, 60, 180 and 540. All processes used N₂ (99.999%) as a carrier gas at a flow rate of 40 standard cubic centimetre per minute (sccm).

The structure and morphology of the MoSe₂/TiO₂ NTs were characterized by field emission scanning electron microscope (FE-SEM JEOL JSM 7500F) and a high-resolution transmission electron microscope (FEI Titan Themis 60, operated at 300 keV) equipped with a high angle annular dark field scanning transmission detector (HAADF-STEM). A proprietary Nanomeasure software was used to measure MoSe₂ interlayer distances and lattice spacing.

The surface chemical composition of MoSe₂ was monitored by X-ray photoelectron spectroscopy (XPS) (ESCA2SR, Scienta-Omicron) using a monochromatic Al K α (1486.7 eV) X-ray source. Due to the strong overlapping of C 1s signal with Se LMM, the binding energy scale was referenced to the binding energy of Mo 3d at 228.3 eV corresponding to MoSe₂.⁶⁵

X-ray diffraction (XRD) analysis was carried out using Panalytical Empyrean with Cu tube and Pixcel3D detector. Grazing incidence XRD was performed to obtain diffraction peaks of the as-deposited MoSe₂. Incident angle was 1 degree. The patterns were recorded in range of 5 – 65°, step size was 0.026 degree.

The diffuse reflectance UV-VIS spectra were recorded in the wavelength range from 200 nm to 900 nm using a UV-VIS spectrophotometer (UV3600Plus Series Shimadzu) with ISR-603 integrating sphere.

Raman measurements were acquired by Raman micro-spectrometer HORIBA LabRAM HR Evolution system coupled by with a confocal microscope. Measurements were taken by 532 nm (green) laser excitation source in the range 100-500 cm⁻¹. All spectra were carefully corrected by baseline correction and noise reduction. Molybdenum selenide powder (Strem, 99.9%) was used as benchmark compound. Spikes were eliminated by spectra accumulation or manually in the LabSpec 6 software.

The photoresponse measurements of MoSe₂/TiO₂ NTs were carried out in an aqueous 0.1 M Na₂SO₄ at 0.4 V vs. Ag/AgCl in the spectral range from 300 to 800 nm. A photoelectric spectrophotometer (Instytut Fotonowy) with a 150 W Xe lamp and a monochromator with a bandwidth of 10 nm connected with a modular electrochemical system AUTOLAB (PGSTAT 204; MetrohmAutolab B. V.; Nova 1.10 software) was used for the photoresponse measurements.

Photocurrent stability tests were carried out by measuring the photocurrent produced under chopped light irradiation (light/dark cycles of 10s).

The photocatalytic degradation activities of all samples were evaluated using photodegradation of methylene blue solution (MB, initial concentration 1×10^{-5} M). Prior to all measurements, to achieve a dye adsorption/desorption equilibrium, the samples were immersed in 3.5 mL of the MB solution for 60 min with constant stirring. Afterwards, the samples were irradiated by a LED-based UV lamp (10 W, $\lambda=365 \text{ nm} \pm 5 \text{ nm}$) and VIS lamp (10 W, $\lambda=410\text{-}425 \text{ nm}$), and the absorbance of the MB solution was periodically measured (10 or 30 min steps) by a UV-VIS spectrometer (S-200, Boeco) at a wavelength of 670 nm to monitor the degradation rate.

The electrocatalytic activity of the different $\text{MoSe}_2/\text{TiO}_2$ NTs catalyst towards HER was examined in a standard three electrode setup by cyclic voltammograms (CV) in 0.5 M H_2SO_4 in the potential range from +0.1 V to -0.8 V vs Ag/AgCl; in 1 M KOH the potential range applied was from +0.1 V to -1.7 V vs Ag/AgCl. The scan rate was 2 mV/s. The first negative scan for all $\text{MoSe}_2/\text{TiO}_2$ NTs layers is shown in the polarization curves.

Chronoamperometry was carried out for the TNT layers coated with 60 cy MoSe_2 in 0.5M H_2SO_4 at -400mV for 26 hours. The potential was chosen more negative than the potential required to deliver a current density of 10 mA in the corresponding polarization curve. The potentials were converted to the reversible hydrogen electrode (RHE) scale by using the following equation:

$$E_{\text{RHE}} = E + (0.059 \text{ V}) \text{ pH} + E_{\text{ref vs SHE}}^0 \quad (1)$$

with $E_{\text{ref vs SHE}}^0 = 0.237 \text{ V}$, being the standard potential of the Ag/AgCl reference electrode vs the standard hydrogen electrode (SHE).

3. Results and discussion

3.1 Characterization

The structure and morphology of the MoSe₂/TiO₂ NT composites were characterized by scanning electron microscopy (SEM), as shown in Figure 1. In the case of TiO₂ NTs decorated with 20 and 60 MoSe₂ ALD cycles, MoSe₂ nanosheets could not be visualized by SEM given their too small dimensions as shown in Figure 1a-b and c-d, respectively. The 180 MoSe₂ ALD cycles samples, exhibited smaller discrete flaky nanosheets homogeneously distributed decorating the TiO₂ NTs surface. The 540 MoSe₂ ALD cycles samples showed flaky MoSe₂ nanosheets with dominant out-of-plane orientation, which covered completely the TiO₂ NTs surface. Overall, SEM top view images in Figure 1 confirmed the presence of flaky MoSe₂ nanosheets within the TiO₂ NTs for 180 and 540 MoSe₂ ALD cycles, respectively. The 20 and 60 MoSe₂ ALD cycles samples were characterized by scanning transmission electron microscopy (STEM) along with the corresponding chemical mapping via energy-dispersive X-ray spectroscopy (EDX). Representative STEM-EDX elemental maps exhibit the chemical distribution of Mo and Se elements on the fragment of a nanotube wall in the cross-sectional view after 20 and 60 MoSe₂ ALD cycles, as shown in Figure 2 a and b, respectively. Homogeneous decoration with MoSe₂ nanosheets was revealed over their entire TiO₂ NTs surface, including the inner bottom parts as showed in Figure S1. A growth rate of ~ 0.083 nm/cy was estimated based on SEM cross-section images in our previous work.⁵⁴ Additional TEM evidence in Figure S2 and S3 (see Supporting Information), corresponding to TiO₂ NTs decorated with 20 and 60 MoSe₂ ALD cycles respectively, provide high-angle annular dark-field (HAADF) STEM images along with complementary EDX elemental maps of the chemical distribution of Ti, O and TiSeMo. Detailed analysis of the as-deposited MoSe₂ nanosheets was carried out also by high-resolution transmission electron microscopy (HR-TEM),

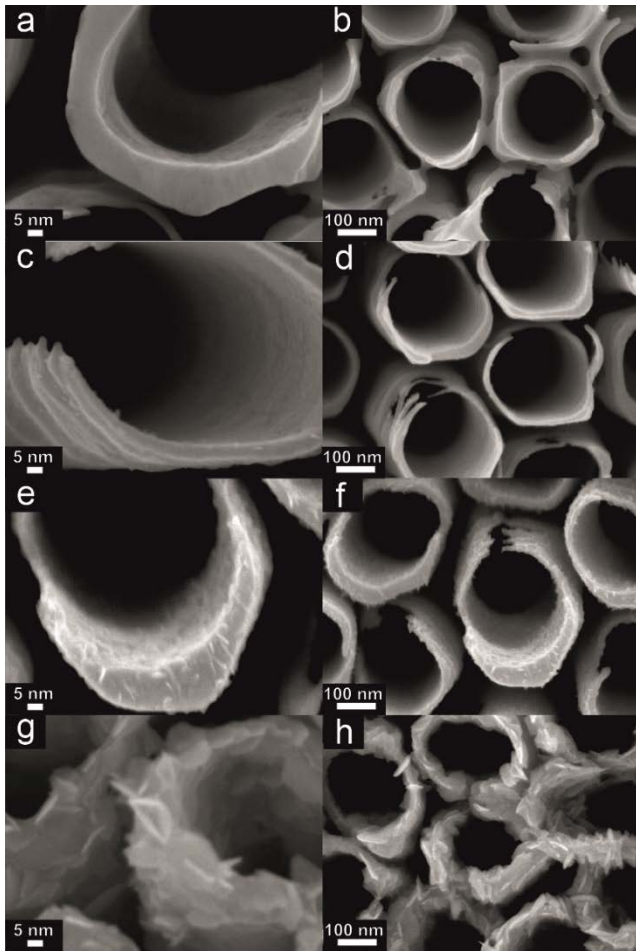


Figure 1. SEM top-view images at two different magnification of TiO₂ NTs decorated with (a-b) 20, (c-d) 60, (e-f) 180 and (g-h) 540 MoSe₂ ALD cycles.

which showed different periodic atom arrangement of the as-deposited MoSe₂ upon 60 ALD cycles, as shown in Figure 2 c-d. The interlayer lattice spacing of 0.28 nm and 0.17 nm were unambiguously ascribed to the (100) and (110) planes, respectively, revealing in-plane hexagonal MoSe₂ growth.³⁸ The hexagonal structure of the as-deposited MoSe₂ was further confirmed by Raman spectroscopy. According to the group theory analysis, hexagonal 2H MoSe₂ structure belongs to the D_{6h} group characterized by four Raman-active modes, three in-plane E_{1g}, E_{2g}¹, and E_{2g}², and one out-of-plane A_{1g}. Figure 3 displays the Raman spectra obtained from the MoSe₂/TiO₂ NTs upon 60, 180 and 540 MoSe₂ ALD cycles. Therein, one can observe characteristic Raman

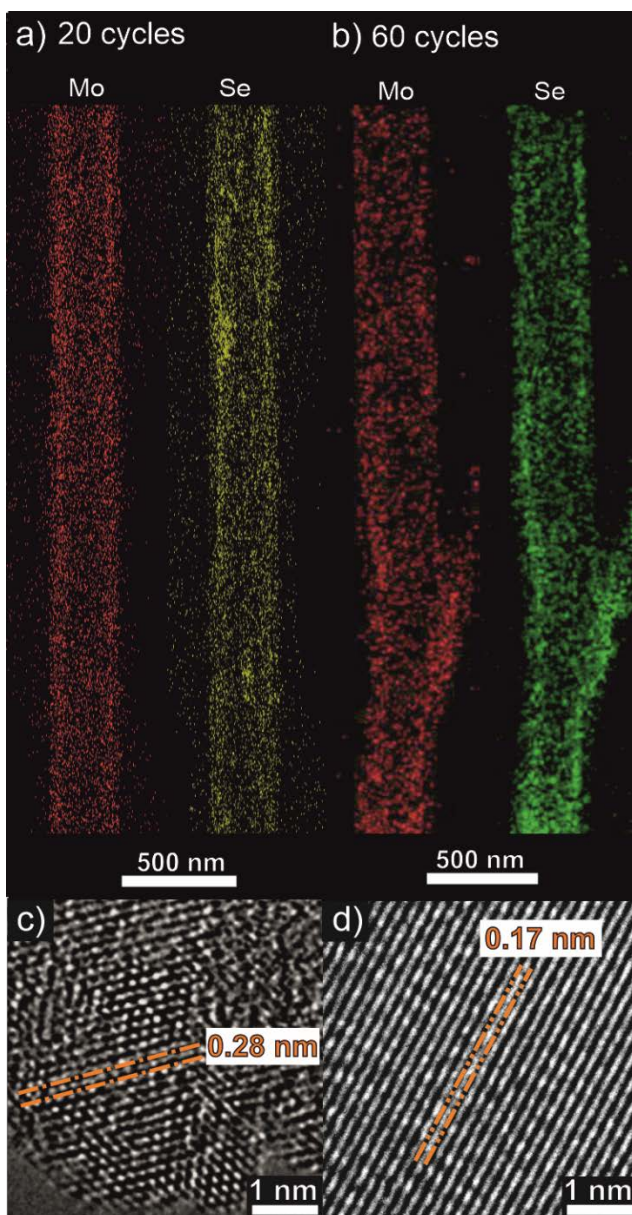


Figure 2. STEM EDX elemental maps show the decoration of Mo and Se species on the TiO₂ NTs wall and reveal a homogeneous MoSe₂ decoration along the TiO₂ NTs wall after (a) 20 and (b) 60 MoSe₂ ALD cycles. High resolution HR-TEM images of MoSe₂ upon 60 ALD cycles displaying interatomic distances (c) of ~ 0.280 nm and (d) ~ 0.17 nm corresponding to the (1 0 0) and (1 1 0) plane of 2H-MoSe₂, respectively.

peaks of MoSe₂: A_{1g} (out-of-plane) and E¹_{2g} (in-plane) modes at ~239 and ~288 cm⁻¹, respectively. The A_{1g} mode exhibited red shift as compared to the peaks position for MoSe₂ powder (242 cm⁻¹), indicating the few-layered nature of the deposited MoSe₂. In addition, a minor peak at ~350 cm⁻¹ observed for the 540 MoSe₂ ALD cycles sample is assigned to the Raman-inactive mode A²_{2u} that becomes active in few-layered 2H-TMDs, as the crystal symmetry along the c-axis is lost. The peak A_{1g} corresponding to 540 MoSe₂ ALD cycles exhibits a shoulder attributed to second order Raman processes.⁵⁴ The intensity of the peaks decreased along with a lower number of MoSe₂ ALD cycles, and could not be detected for the 20 MoSe₂ ALD cycles sample (not showed here). The multiple lattice vibrational modes of MoSe₂ suggested the 2H hexagonal polycrystalline nature of the MoSe₂. The prevailing out-of-plane orientation over in-plane orientation of the MoSe₂ nanosheets was confirmed by the difference in the relative intensities between the A_{1g} and E¹_{2g} modes observed herein for 180 and 540 MoSe₂ ALD cycles samples, as described in previous works.⁴³

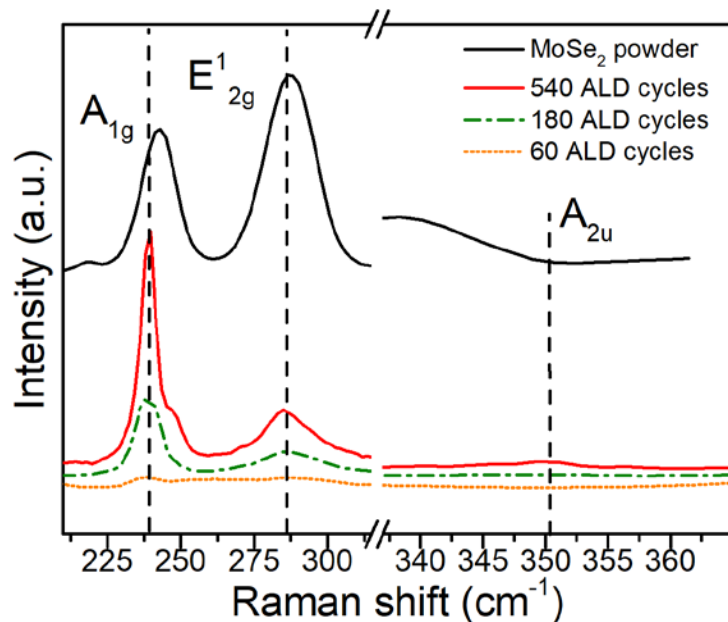


Figure 3. Raman spectra obtained from MoSe₂ powder and MoSe₂/1D TiO₂ NTs upon depositing 60, 180 and 540 MoSe₂ ALD cycles.

The characterization carried out by Grazing Incident X-Ray Diffractometry (GI-XRD) confirmed the 2H hexagonal polycrystalline nature of the as-deposited MoSe₂. The GI-XRD patterns (Figure S4) obtained from TiO₂ NTs with 180 and 540 MoSe₂ ALD cycles exhibited diffraction peaks at $2\theta \sim 13.3^\circ$ and $\sim 31^\circ$, which matched well with the (002) and (100) planes of hexagonal (2H) MoSe₂ indicating the high purity of the as-deposited MoSe₂. The planes (002) and (100) also confirmed the coexistence of MoSe₂ with out-of-plane and in-plane orientation in the case of samples with 180 and 540 ALD MoSe₂ cycles. GI-XRD patterns corresponding to TiO₂ NTs decorated with 60 (Figure S4) and 20 (data not shown) MoSe₂ ALD cycles only exhibited TiO₂ anatase diffraction peaks. The lack of MoSe₂ diffraction peaks was ascribed to the small crystalline domains of the MoSe₂ comprising the nanosheets synthesized upon such number of ALD cycles.

The surface chemical composition of the as deposited MoSe₂ nanosheets was analysed by X-Ray Photoelectron Spectroscopy (XPS) at first. Figure S5 shows the XPS survey spectra for the different number of ALD cycles, where the absence of other chemical species indicates the high purity of the as-deposited ALD MoSe₂. Due to the strong overlapping of C 1s signal with Se LMM, the use of adventitious carbon (284.8 eV) as a reference to adjust the binding energy scale was not reliable. As an alternative, the binding energy of Mo 3d at 228.3 eV corresponding to MoSe₂ was used for this purpose.⁶⁵ The left column of Figure 4 shows the deconvolution of the XPS high resolution spectra of Mo 3d obtained from the TiO₂ NTs decorated with 5, 20, 60, 180 and 540 MoSe₂ ALD cycles. This deconvolution allowed to obtain a meaningful insight into the chemical composition of the ALD MoSe₂/TiO₂ NTs surface, in particular for the low-cycle ALD processes (5, 20 and 60 ALD cycles). Peak corresponding to the presence of Mo-Se-O bonds $\sim 229.9\text{eV}$ (Mo3d5/2) was pivotal, as it verified the chemical reaction of both the Se precursor with the

hydroxyl groups and the subsequent reaction of the resulting chemisorbed counterpart with the Mo precursor. Besides, the lack of Mo-Cl species and the absence of chlorine residues indicated a complete ligand exchange reaction between MoCl₅ and (Me₃Si)₂Se, yielding desired MoSe₂ structure.⁵⁵ The absence of chlorine residues was also confirmed by the XPS survey spectra results in Figure S3. Mo(IV)-Se exhibited two peaks at 228.3 and 231.4 eV corresponding to spin-orbit splitting Mo 3d_{5/2} and Mo 3d_{3/2} corroborating the growth of MoSe₂. Additional peaks were revealed with binding energies (BE) corresponding to different chemical environment. These peaks fitted well with the presence of Mo-O-Ti bonds at ~231eV (Mo3d_{5/2}) and Mo(VI)-O bonds at ~232.3eV (Mo3d_{5/2}), ascribed to a substrate interface effect stemming from the low-cycle ALD stage. Even though the Se precursor was first introduced in the chamber remaining available hydroxyl groups from the TiO₂ NTs surface reacted with MoCl₅ as it was introduced into the

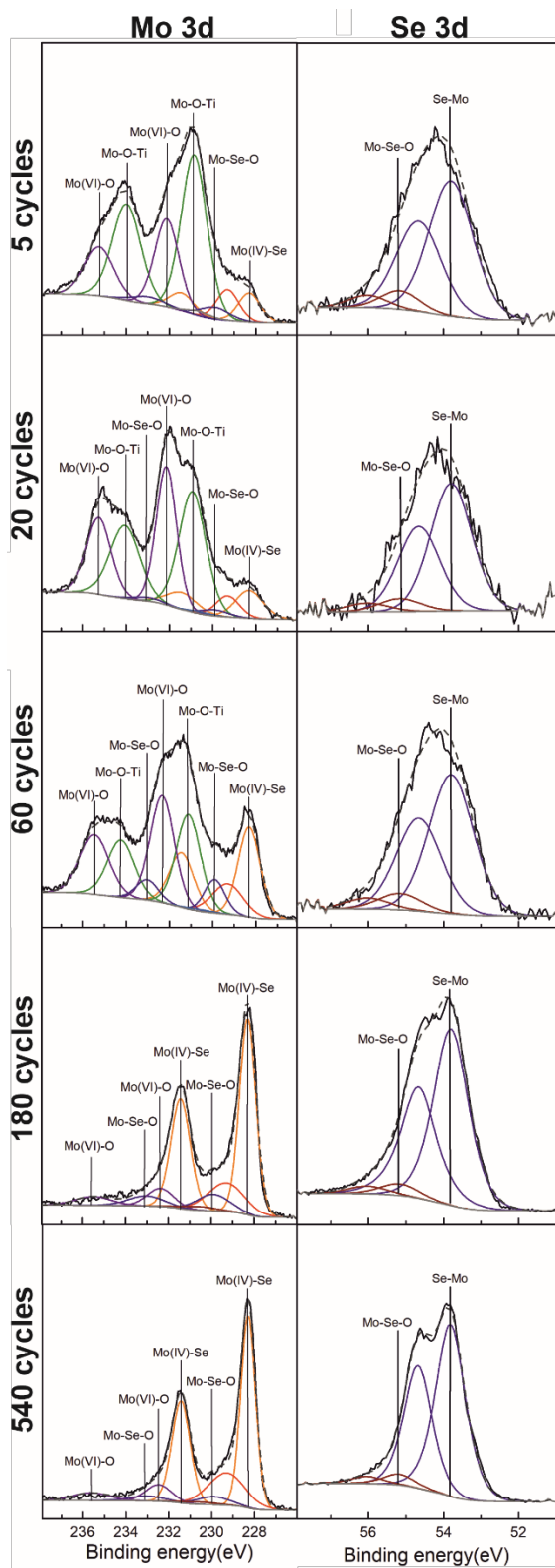


Figure 4. XPS high-resolution spectra of Mo 3d and Se 3d deconvoluted peaks corresponding to 5, 20, 60, 180 and 540 MoSe₂ ALD cycles.

chamber and in line with observations in a recent work.⁵⁵ The strong fading of such peaks observed along with the increasing number of ALD cycles, suggested that the formation of embedded MoO_x species within the MoSe₂ was limited to a substrate interface effect (the only source of hydroxyl groups). The right column of Figure 4 shows corresponding deconvoluted XPS high resolution spectra of Se 3d. This deconvolution enabled identifying the presence of i) Mo-Se-O bonds at BE values confirming the successful chemical reaction between both Se and Mo precursors as mentioned above, and ii) two main Se-Mo peaks located at 54.6 and 53.8 eV attributed to Se 3d_{3/2} and Se 3d_{5/2} of 2H MoSe₂. Additionally, the XPS spectra of O and Ti (Figure S6) show decreasing intensity of the characteristic Ti and O peaks along with the increasing number of MoSe₂ ALD cycles, also observable in the XPS survey spectra (see Figure S5). The obvious cause of such intensity attenuation is the MoSe₂ nanosheets growing on the TiO₂ NTs surface along with the number of ALD cycles.

3.2 Photoelectrochemical properties

The photoelectrochemical properties of blank and ALD MoSe₂/TiO₂ NTs were analysed in the wavelength range from 300 nm to 800 nm. The corresponding incident photon-to-electron conversion efficiency values (IPCE) are shown in Figure S7a. In the UV region TiO₂ NTs layers decorated with 5 and 20 MoSe₂ ALD cycles displayed significantly higher IPCE values (up to 58% and 30% respectively) in comparison with blank counterpart (up to 16%) in the range of 300-360 nm. This is due to the effective passivation of the surface defects (oxygen vacancies and traps) within the TiO₂ nanotube walls upon low-cycle MoSe₂ ALD stage, leading to a lower recombination rate and more efficient charge carrier separation.⁶⁶⁻⁶⁸ In the visible spectral region blank TiO₂ NTs exhibited no photoresponse due to the high band gap energy of anatase TiO₂ E_g~3.2 eV (≈ 387 nm), while TiO₂ NTs decorated with 5, 20 and 60 MoSe₂ ALD cycles extended

the photoresponse significantly. The corresponding photoresponse indicated longer lifetimes (lower recombination rate) of the photo-generated charge carriers, resulting in a more effective separation, transfer and collection of the charge carriers. The band offset at the MoSe₂/TiO₂ interface and the associated built-in electric field accounted for more efficient charge carrier separation, as compared to the blank nanotubes. Nevertheless, it was also observed that a higher number of MoSe₂ ALD cycles (60 and 180) yielded inferior photoelectrochemical properties in both spectral regions, i.e. lower IPCE values, which can mainly be ascribed to enlarged thickness/size of the MoSe₂ nanosheets (as seen on SEM; Figure 1). It must be considered that the growing number of stacking MoSe₂ layers negatively affect the inherent low electron conductivity in perpendicular direction to the basal MoSe₂ planes, as well as the charge carrier separation efficiency. These effects significantly intensified for TiO₂ NTs deposited with 180 MoSe₂ ALD cycles, whose photoresponse was significantly suppressed. A similar shading effect was reported in our earlier published work based on TiO₂ NTs decorated with ALD MoS₂ nanosheets.⁶²

Photocurrent transients in Figure S7b were recorded over a range of wavelengths both in UV (350-370 nm) and visible (410-430 nm) region to evaluate the separation efficiency of the photo-generated charge carriers. The photocurrent response for TiO₂ NTs decorated with 5 and 20 MoSe₂ ALD cycles was higher than that of the blank counterpart. That, together with the sharp photocurrent density increase/drop under ON/OFF irradiation cycles, both in the UV and visible light regions, verified the improved charge carrier separation efficiency. Nevertheless, an increase in the number of ALD cycles (60 and 180) brought about lower photocurrent density and a characteristic delay in time photoresponse as the irradiation is turned ON/OFF, as result of charge recombination and sluggish charge transport kinetics. These results matched well with the

detrimental effects on the charge carriers transport described above resulting from a higher number of MoSe₂ ALD cycles and the consequent growth of the MoSe₂ nanosheets.

3.3 Optical properties

As the light absorption property is a key factor to determine the photocatalytic properties, the optical properties were further evaluated by diffuse reflectance spectroscopy measurements, as shown in Figure S8a. The resulting diffuse reflectance spectra of the MoSe₂/TiO₂ NTs clearly exhibit how the optical absorption ability increased, as compared to their blank counterpart in the visible light region in parallel with the number of MoSe₂ ALD cycles. The Kubelka-Munk function $F(R) = \alpha = (1-R)^2 / 2R$ (R is the reflected light percentage and α is absorption coefficient) was used to estimate the effect of the number of MoSe₂ ALD cycles on the optical band gap energy (see Figure S8b). The band gap energy was calculated using the Tauc equation, $\alpha h\nu = C (h\nu - E_g)^{n/2}$, where α is the absorption coefficient, h is Planck constant, ν is the light frequency, E_g is the band gap energy, C is a constant, and the coefficient n is $n=1$ for direct transition and $n=4$ for indirect transition in a semiconductor. In the present case, $n=4$ was used as the base of the studied materials is TiO₂, which is indirect semiconductor. Tauc equation could not be applied for the 180 and 540 MoSe₂ ALD cycles samples, as they were too much light absorbing. The optical band gap values, estimated by the x-axis intercept, were 3.01 eV (blank), 2.98 eV (20 cycles) and 2.76 eV (60 cycles) indicating the strong influence of the number of MoSe₂ ALD cycles on the band gap value and the light absorbance ability. All in all, the results clearly indicated that the optical properties of the MoSe₂/TiO₂ NTs were significantly determined by the number of MoSe₂ ALD cycles.

3.4 Photocatalytic properties

The photocatalytic activity assessment of the different MoSe₂/TiO₂ NTs was carried out monitoring the photodegradation of methylene blue solution (MB), as model organic dye, under UV (365 nm) and visible light irradiation (410-425 nm). Figure 5a exhibits, how the photocatalytic activity improved under UV light (365 nm) with the number of MoSe₂ ALD cycles deposited on the TiO₂ NTs, exhibiting pseudo-first order degradation kinetic. The corresponding photocatalytic kinetic rate constants (shown in Table 1) were obtained from the linear fitting of the curves (dashed lines):

$$\ln (C/C_0) = k t \quad (2)$$

where C_0 and C are MB concentrations at the beginning and at time t , respectively, and k is the pseudo-first order kinetic rate constant.

Table 1. Photocatalytic (pseudo-first order) kinetic rate constants (k) of MB degradation upon UV illumination (365 nm, LED array) for blank TiO₂ NTs and MoSe₂ decorated ones with different number of MoSe₂ ALD cycles. The kinetics rate constant values were obtained by linear fitting of the curves exhibited in Figure 7a.

Sample	k (min⁻¹)
Blank	0.0279
20 ALD cycles	0.0340
60 ALD cycles	0.0487
180 ALD cycles	0.0471
540 ALD cycles	0.0297

The MB concentration after 60 minutes for the blank TiO₂ NTs, and TiO₂ NTs decorated with 20, 60, 180 and 540 MoSe₂ ALD cycles was reduced to 25.0%, 12.4%, 5.5% , 5.4% and 16.5% of

its initial value, respectively. Those results verified the synergistic effect stemming from the composite nanotubular structure rendering outstanding photocatalytic properties, with MB degradation rates enhanced up to five times, as compared to the blank counterpart. Higher light absorption (as shown in Figure S8 for MoSe₂/TiO₂ NTs) and improved separation efficiency resulted in greater available active species, generated from the photoexcited catalysts at the electrolyte-MoSe₂/TiO₂ NTs interface that essentially boosted the photocatalytic properties. Interestingly, a strong shading effect of the TiO₂ NTs surface upon the deposition of 540 MoSe₂ cycles resulted in detrimental for the UV photocatalytic performance. The large MoSe₂ nanosheets significantly reduced the TiO₂ NTs surface available to absorb UV light driving to a significant drop of the overall photocatalytic performance. One must notice that under UV irradiation both TiO₂ and MoSe₂ exhibit catalytic activity. Therefore, in order to evaluate the photocatalytic activity of the MoSe₂ nanosheets, MB degradation was performed under visible light illumination, where TiO₂ is catalytically inactive (due to its wider band-gap). The results in Figure 5b displayed the MB degradation under visible light irradiation (410-425 nm). The MB concentration after 120 minutes for TiO₂ NTs decorated with 20, 60, 180 and 540 MoSe₂ ALD cycles was reduced to 25.5%, 12.1%, 8.3% and 5.4% of its initial value, respectively. Interestingly, the deviation from first-pseudo order kinetics was observed for TiO₂ NTs decorated with 20, 60 MoSe₂ ALD cycles (see Figure 5b).

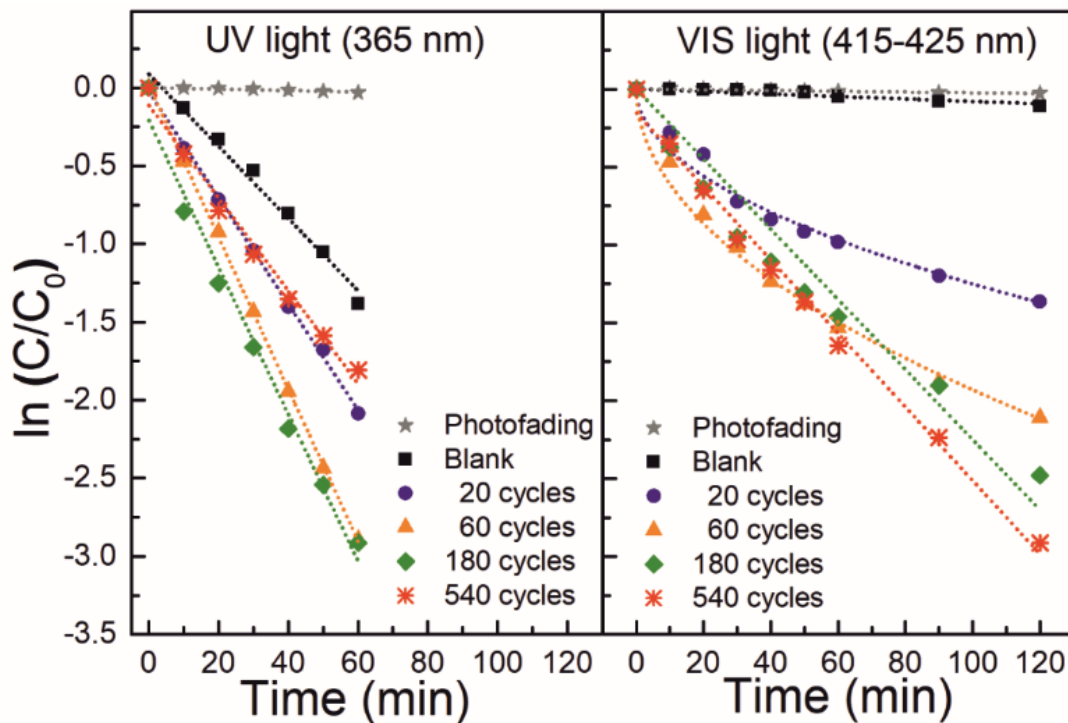


Figure 5. Photocatalytic decomposition rates of MB for blank and TiO₂ NTs decorated with 20, 60, 180 and 540 MoSe₂ ALD cycles using (a) UV light (365 nm) and (b) VIS light (415-425 nm).

Such behavior was already observed in vertically oriented MoSe₂ nanosheets grown on reduced graphene oxide heterostructure for photocatalysis.⁶⁹ Unfortunately, no description of such deviation was provided in that work. In order to determine the origin of the first-pseudo order kinetics deviation, the progressive MoSe₂ photodegradation under the visible light illumination was firstly considered. The MoSe₂ photostability under visible light illumination was assessed by reproducing photocatalytic experimental conditions by immersing a MoSe₂/TiO₂ NTs sample in distilled water for 1 h in the dark, subsequently irradiated for 2 hours by a photoelectric spectrophotometer with a 150 W Xe lamp at a wavelength of 420 nm (i.e. similar wavelength used for visible light photocatalysis). XPS high resolution spectra of Mo 3d and Se 3d conducted before and after the experiment (see Figure S9) revealed no (photo)degradation, which fully confirmed the sufficient MoSe₂ photostability in an aqueous solution. Therefore, (photo)degradation could be

ruled out from the evaluation. An additional approach, aiming to describe the first-pseudo order kinetics deviation, consisted of a simple mathematical expression containing the MB degradation rate and time as dependent and independent variable, respectively. Using this approach, the experimental results (for 20 and 60 MoSe₂ ALD cycles samples) were found to exhibit a \sqrt{t} time dependence following the next expression:

$$\ln (C/C_0) = -A \sqrt{t} \quad (3)$$

where $\ln (C/C_0)$ is the MB degradation rate as in equation 2 and A is a coefficient, whose value allows best curve fitting. As $\ln (C/C_0)$ is non-dimensional, it means that the units of coefficient A must be $\text{min}^{-1/2}$. Then, the coefficient A^2 (with the same units as a reaction rate coefficient of first order, i.e. min^{-1}) would be related to the degradation rate, and its potential physical interpretation would relate to the number of available MoSe₂ catalytic active sites. The corresponding values of the coefficient A^2 are shown in the Table S1.

Given the good fitting of the experimental results to equation 3, a rational description of the photocatalytic results can be put forward based on two facts that come into play: i) under the visible light illumination the catalytically active sites are confined to the MoSe₂ active edges (TiO₂ is not catalytically active under visible light), which strongly reduces the available catalytically active surface area; ii) the 1D nanotubular morphology inhibits partly the mass transport towards MoSe₂ catalytically active sites.

Assuming these facts, a diffusion-controlled process was considered, where surface reactions (MB adsorption/desorption processes) influence the overall rate and possess the rate determining step in the photocatalysis under visible illumination for 20 and 60 MoSe₂ ALD cycle samples. This is especially pronounced, when the MB concentration decreases after some tens of minutes of illumination (displayed by the deviation from the pseudo-first order kinetics). Thus, when a MB molecule (of a low MB solution concentration) at the very surface of a particular available MoSe₂

nanosheet gets decomposed (to some by-products), new MB molecule needs longer time to adsorb there and get decomposed, compared to situation of high MB concentration and high number of catalytically active sites. This explains the deviation from the pseudo-first kinetics. Remarkably, in the case of 180 and 540 MoSe₂ ALD cycles, experimental data showed better fitting using linear regression, i.e. the MB degradation process was closer to follow pseudo-first order degradation kinetic. Someway, it could be expected, as upon 180 and 540 MoSe₂ ALD cycles, TiO₂ NTs surface is mostly covered by MoSe₂ nanosheet that provide their active sites for the MB reduction. In parallel, one can expect that larger MoSe₂ nanosheets offer higher number of catalytic sites leading to superior photocatalytic performance, as exhibited by the TiO₂ NTs with 180 and 540 MoSe₂ ALD cycles.

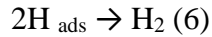
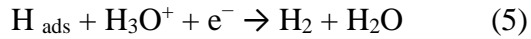
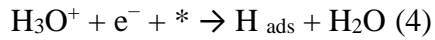
As to the chemical and physical stability of the MoSe₂/TiO₂ NTs after photocatalytic performance, it was evaluated and verified by XPS and SEM analysis respectively, as shown in Figure S10. XPS analysis (Figure S10a) revealed good chemical MoSe₂ stability exhibiting a very minor oxidation, while SEM images (Figure S10 b-c) confirmed the physical stability of both the TiO₂ NTs and the MoSe₂ nanosheets. The photocatalytic performance of ALD MoSe₂/TiO₂ NTs was found superior as compared to different works in the literature, reporting degradation of MB on various MoSe₂ nanostructured surfaces, as shown in Table S2, always considering that that the results compared were measured under different experimental conditions.

3.5 Electrocatalytic properties

As already mentioned in the introduction, the Gibbs free energy for H₂ adsorption on MoSe₂ edges, estimated by theoretical calculations, is close to zero, which leads to a high hydrogen adsorption. Therefore, the hydrogen evolution reaction (HER) catalytic activity of the MoSe₂/TiO₂

NTs decorated with different number of ALD MoSe₂ cycles was studied both in acidic (0.5 M H₂SO₄) and alkaline (1 M KOH) solutions using a three-electrode electrochemical cell set-up. The current densities were normalized to the macroscopic surface area of the samples exposed to the solution and potentials were quoted against the reversible hydrogen electrode (RHE).

Regarding the HER process in acidic solution, the adsorbed hydrogen is formed in a first step via the reduction of hydronium ion (H₃O⁺) on an active site of the catalyst in the discharge step or Volmer reaction (equation 4), followed by the formation of molecular H₂, which can proceed either through an electrochemical desorption via the transfer of a second hydronium ion (Heyrovsky step, equation 5) or by the recombination of two adsorbed protons (Tafel step, equation 6):



where * denotes an active site on the catalyst surface and H_{ads} an adsorbed hydrogen atom on a catalyst active site. Figure 6a displays the HER polarization curves within a cathodic potential window obtained in 0.5 M H₂SO₄ solution. The overpotential values required to deliver a current density of 10 mA cm⁻² decreased considerably related to the blank TiO₂ NTs, confirming, that the incorporation of MoSe₂ significantly enhanced the electrocatalytic properties. The corresponding overpotential and Tafel slope values are displayed in Table 2.

Table 2. Overpotential at the cathodic current density of 10 mA cm⁻² and Tafel slope obtained for the TiO₂ NTs decorated with different number of MoSe₂ ALD cycles in 0.5 M H₂SO₄ solution.

Sample	Overpotential (mV)	Tafel slope (mV/dec)
20 ALD cycles	302	101
60 ALD cycles	261	96

180 ALD cycles	229	75
540 ALD cycles	258	76

Principally, a higher number of MoSe₂ ALD cycles brought about lower overpotential and Tafel slope values. It indicated an improvement of the HER rate, which was ascribed to the increasing number of MoSe₂ edges sites (active catalytic sites) offered by larger MoSe₂ nanosheets. Unexpectedly, the sample containing 540 MoSe₂ ALD cycles exhibited an increasing overpotential value with respect to the sample with 180 MoSe₂ ALD cycles, indicating lower electrical conductivity and ascribed to larger MoSe₂ nanosheets composed of a higher number of stacked layers. In parallel, the kinetics rate did not show an improvement as one could expect related to a higher number of edges active catalytic sites. As shown in Figure 6b, the lowest Tafel slope of 75 mV/dec was obtained from the TiO₂ NTs deposited with 180 MoSe₂ ALD cycles. The reason behind could be similar to those described above, i.e. that despite offering higher number of edges sites due to the significantly larger size of the MoSe₂ nanosheets (upon 540 ALD cycles), the access/availability to the edge sites could be limited due the nanosheet morphology. The random growth of the MoSe₂ nanosheets (vertically/planar oriented) disables the access to some catalytic active edges (that remain passive), and has a negative impact on the transport of reactants and by-products through (i.e. there are mass diffusion limitations). Then, the reaction rate could be mainly limited by the accessibility to catalyst active sites and mass diffusion limited of reactants and byproducts.

Outstanding electrochemical stability of the MoSe₂/TiO₂ NTs was demonstrated after 300 CV cycles as shown in Figure 6c. In addition, chronoamperometric measurements were conducted for a more exhaustive assessment of the long-term stability of ALD MoSe₂/TiO₂ NTs in 0.5 M H₂SO₄ by applying a constant overpotential value of -400 mV for 26 hours, as shown in Figure 6d. The

long-term stability of the catalyst was confirmed showing a good current density retention verifying the electrochemical stability of the MoSe₂/TiO₂ NTs. The physical stability of the MoSe₂/TiO₂ NTs after electrocatalytic performance was confirmed by SEM images (Figure S11 a-b) where one can observe the total integrity of both the TiO₂ NTs and the MoSe₂ nanosheets.

Table S4 exhibits a comparison of characteristic HER catalytic parameters reported for a set of heteronanostructures based on MoSe₂ as (co)catalyst employing different supporting materials.

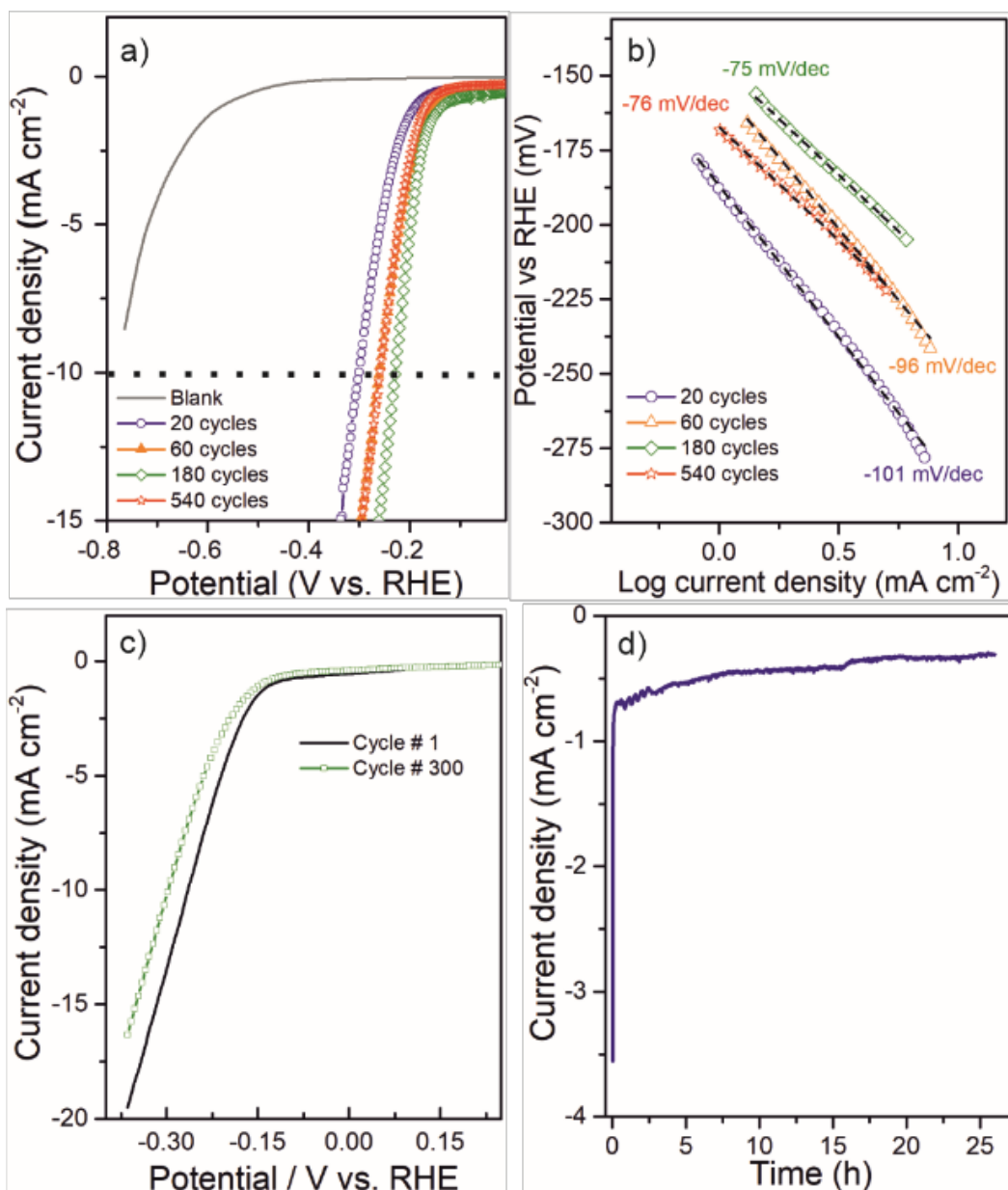


Figure 6. (a) HER polarization curves obtained for TiO₂ NTs decorated with different number of MoSe₂ ALD cycles and (b) the corresponding Tafel plots in 0.5M H₂SO₄ solution. (c) LSV polarization curves corresponding to 1st and 300th CVs, obtained using TiO₂ NTs decorated with 180 MoSe₂ ALD cycles. (d) Retention current density conducted over 26 hours applying an overpotential value of -400 mV using TiO₂ NTs decorated with 60 MoSe₂ ALD cycles.

In order to obtain a complete evaluation on the catalytic ability of the different samples, the HER catalytic activity was performed in alkaline solution (1 M KOH). Unlike in acidic solution, in alkaline solution the water molecule plays the role of hydronium ion. As the first step is the water dissociation, the HER is usually two or three orders of magnitude slower than in acidic solution:

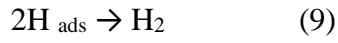
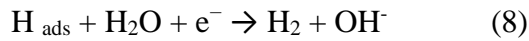


Figure S12a and b display the HER polarization curves within a cathodic potential window and the corresponding Tafel slopes obtained in 1 M KOH solution, respectively. Similar to results obtained in the acidic solution, the overpotential values, required to deliver a current density of 10 mA cm⁻², diminished considerably as compared to blank TiO₂ NTs. That suggest a higher number of catalytic active sites provided by the MoSe₂ enhance significantly the electrocatalytic properties. Nevertheless, the lowest Tafel slope, was exhibited by the sample with lowest number of MoSe₂ ALD cycles (20 cycles), which, in turn, offered the highest anatase TiO₂ (101) available surface. The ability of anatase TiO₂ (101) to adsorb and dissociate water must be noted and would suggest that in alkaline solution anatase TiO₂ could play an important role in HER process.⁷⁰ Thus, the preferential mechanism for water dissociation on anatase TiO₂ (101) surface is found to be the splitting of the H-OH bond, what is the first step of the HER in alkaline solution. Therefore, higher

available anatase TiO₂ (101) surface would trigger the HER process in accordance with the results observed. The corresponding overpotential and Tafel slope values are displayed in Table S3.

However, fast catalytic performance decay was depicted by overpotential shift towards more negative values after several consecutive CV cycles as displayed in Figure S12c. The sample showed clear visual differences as shown in Figure S12d. The sample surface area in contact with the alkaline solution (denoted by blue dashed line in Figure S12d) turned brighter. Meaningful insights on the surface chemistry changes occurring during the HER was provided by XPS analysis (see Figure S11c). Therein, the high-resolution spectra of Mo 3d peaks provides an important information on the electrochemical stability of the MoSe₂ both in acidic (0.5 M H₂SO₄) and alkaline solution (1 M KOH). Whereas MoSe₂ was electrochemically stable after 300 CVs in 0.5 M H₂SO₄, a clear oxidation process, confirmed by the presence of a peak at ~ 236 eV and a shoulder at ~ 232.5 eV, occurred upon only 3 CVs in 1M KOH. Therefore, long-term electrochemical stability can be expected from MoSe₂ in acidic solution, while fast MoSe₂ degradation (oxidation) was found in alkaline solution.

4. Conclusions

A simple fabrication of MoSe₂/1D TiO₂ NTs heterostructures by incorporating different number of MoSe₂ ALD cycles on TiO₂ NTs was presented in this work. The MoSe₂ nanosheets grow vertically aligned maximizing the exposed active edges, a pivotal feature for catalysis performance. Therefore, the photoelectrochemical and catalytic properties of ALD MoSe₂/1D TiO₂ NTs were assessed for hydrogen evolution reaction and dye organic pollutant degradation applications respectively, as a function of the number of MoSe₂ ALD cycles by which a precise control over MoSe₂ nanosheet can be attained. The photoelectrochemical and catalytic properties displayed an important dependence on the number of MoSe₂ ALD cycles, and verified the

synergistic effect stemming from the MoSe₂ growth within TiO₂ NTs. Hence, remarkable results have been obtained both in photo- and electrocatalysis from a rather simple heterostructure, confirming the ALD MoSe₂/TiO₂ NTs as an excellent nanostructure towards photoelectrochemical, photocatalytic and electrocatalytic applications.

ASSOCIATED CONTENT

Supporting Information available: Figure S1, SEM images of the bottom part of TiO₂ NTs decorated with 540 MoSe₂ ALD cycles. Figures S2-S3, High-angle annular dark field STEM image of TiO₂ NTs decorated with 20 and 60 MoSe₂ ALD cycles, together with the corresponding EDX elemental maps of the chemical distribution of Ti, O and TiSeMo. Figure S4, XRD patterns of annealed blank TiO₂ NTs and TiO₂ NTs decorated with 60, 180 and 540 MoSe₂ ALD cycles.. Figure S5, XPS survey spectra of the TiO₂ NTs decorated with 5, 20, 60, 180 and 540 MoSe₂ ALD cycles. Figure S6, XPS high-resolution spectra of Ti 2p and O 1s corresponding to the TiO₂ NTs decorated with 5, 20, 60, 180 and 540 MoSe₂ ALD cycles. Figure S7, incident photon-to-electron conversion efficiency (IPCE) vs wavelength, and (b) photocurrent transients for the blank and TiO₂ NTs decorated with different number of MoSe₂ ALD cycles. Figure S8, diffuse reflectance spectra for the blank TiO₂ NTs and TiO₂ NTs decorated with 20, 60 and 180 MoSe₂ ALD cycles and transformed Kubelka-Munk spectra for 20 and 60 cycle samples. Figure S9, XPS high-resolution spectra of Mo 3d deconvoluted and Se 3d peaks corresponding to TiO₂ NTs decorated with 360 MoSe₂ ALD cycles before and after conducting the photostability test. Figure S10, XPS high-resolution spectra of Mo 3d peaks corresponding to 180 MoSe₂ ALD cycles TiO₂ NTs samples as-deposited and after photocatalytic performance; SEM images after photocatalytic performance. Figure S11, SEM images of TiO₂ NTs decorated with 540 MoSe₂ ALD cycles after electrocatalytic

performance in 0.5 M H₂SO₄; XPS high-resolution spectra of Mo 3d peaks corresponding to 180 MoSe₂ ALD cycles TiO₂ NTs samples with MoSe₂ as-deposited, after 300 CVs in 0.5 M H₂SO₄, and after 3 CVs in 1 M KOH. Figure S12, HER polarization curves obtained for TiO₂ NTs decorated with different number of MoSe₂ ALD cycles and the corresponding Tafel plots in 1 M KOH. HER polarization curves obtained for TiO₂ NTs decorated with 180 MoSe₂ ALD cycles corresponding to three consecutive CVs. Optical picture of one sample upon several CVs in 1 M KOH. Table S1, coefficient A² (for TiO₂ NTs with 20 and 60 MoSe₂ ALD cycles) and constant (k) values (for TiO₂ NTs with 180 and 540 MoSe₂ ALD cycles) of MB degradation upon the visible light illumination. Table S2, photocatalytic performance of MoSe₂ reported in literature for methylene blue degradation. Table S3, overpotential and Tafel slope values obtained for the TiO₂ NTs decorated with different number of MoSe₂ ALD cycles in 1 M KOH solution.

This material is available free of charge via the Internet at <http://pubs.acs.org>.

AUTHOR INFORMATION

Corresponding Author

* Raul Zazpe - Center of Materials and Nanotechnologies, Faculty of Chemical Technology, University of Pardubice, Nam. Cs. Legii 565, 530 02 Pardubice, Czech Republic; Central European Institute of Technology, Brno University of Technology, Purkynova 123, 612 00 Brno, Czech Republic; Email: raul.zazpe@upce.cz

ORCID IDs

Raul Zazpe 0000-0003-0017-2323

Richard Krumpolec 0000-0003-4432-2717

Hanna Sopha 0000-0001-7144-5427

Jhonatan Rodriguez-Pereira 0000-0001-6501-9536

Jaroslav Charvot 0000-0002-7811-015X

Ludek Hromadko 0000-0001-9540-5833

Eva Kolibalova 0000-0002-8548-8185

Jan Michalicka 0000-0001-6231-0061

David Pavlinak 0000-0001-9669-7946

Martin Motola 0000-0001-7394-9944

Milos Krbal 0000-0002-8317-924X

Jan Prikryl 0000-0002-1572-7216

Filip Bures 0000-0002-2832-6673

Jan M. Macak 0000-0001-7091-3022

Author Contributions

The manuscript was written through contributions of all authors. All authors have given approval to the final version of the manuscript.

Notes

The authors declare no competing financial interest

ACKNOWLEDGMENT

The authors acknowledge the financial support from the Czech Science Foundation (18-03881S), and the Ministry of Education, Youth and Sports of the Czech Republic (MEYS CR, projects LO1411, LQ1601, LM2018103). TEM analyses were carried out with the support of CEITEC Nano Research Infrastructure (LM 2018110, MEYS CR, 2020-2022).

REFERENCES

- (1) Pirkanniemi, K.; Sillanpää, M. Heterogeneous Water Phase Catalysis as an Environmental Application: A Review. *Chemosphere* **2002**, *48* (10), 1047–1060. [https://doi.org/10.1016/S0045-6535\(02\)00168-6](https://doi.org/10.1016/S0045-6535(02)00168-6).
- (2) Centi, G.; Perathoner, S. Catalysis and Sustainable (Green) Chemistry. *Catal. Today* **2003**, *77* (4), 287–297. [https://doi.org/10.1016/S0920-5861\(02\)00374-7](https://doi.org/10.1016/S0920-5861(02)00374-7).
- (3) Dubouis, N.; Grimaud, A. The Hydrogen Evolution Reaction: From Material to Interfacial Descriptors. *Chem. Sci.* **2019**, *10* (40), 9165–9181. <https://doi.org/10.1039/c9sc03831k>.
- (4) Sheldon, R. A. Engineering a More Sustainable World through Catalysis and Green Chemistry. *J. R. Soc. Interface* **2016**, *13* (116), 20160087. <https://doi.org/10.1098/rsif.2016.0087>.
- (5) Manzeli, S.; Ovchinnikov, D.; Pasquier, D.; Yazyev, O. V.; Kis, A. 2D Transition Metal Dichalcogenides. *Nat. Rev. Mater.* **2017**, *2* (8), 17033. <https://doi.org/10.1038/natrevmats.2017.33>.
- (6) Wang, Q. H.; Kalantar-Zadeh, K.; Kis, A.; Coleman, J. N.; Strano, M. S. Electronics and Optoelectronics of Two-Dimensional Transition Metal Dichalcogenides. *Nat. Nanotechnol.* **2012**, *7* (11), 699–712. <https://doi.org/10.1038/nnano.2012.193>.

- (7) Mak, K. F.; Shan, J. Photonics and Optoelectronics of 2D Semiconductor Transition Metal Dichalcogenides. *Nat. Photonics* **2016**, *10* (4), 216–226. <https://doi.org/10.1038/nphoton.2015.282>.
- (8) Ping, J.; Fan, Z.; Sindoro, M.; Ying, Y.; Zhang, H. Recent Advances in Sensing Applications of Two-Dimensional Transition Metal Dichalcogenide Nanosheets and Their Composites. *Adv. Funct. Mater.* **2017**, *27* (19), 1605817. <https://doi.org/10.1002/adfm.201605817>.
- (9) Pumera, M.; Sofer, Z.; Ambrosi, A. Layered Transition Metal Dichalcogenides for Electrochemical Energy Generation and Storage. *J. Mater. Chem. A* **2014**, *2* (24), 8981–8987. <https://doi.org/10.1039/C4TA00652F>.
- (10) Li, H. H. H.; Shi, Y.; Chiu, M. H.; Li, L. J.; Lu, Q.; Yu, Y.; Ma, Q.; Chen, B.; Zhang, H.; Jin, H.; Guo, C.; Liu, X.; Liu, J.; Vasile, A.; Jiao, Y.; Zheng, Y.; Qiao, S.; Li, Z.; Wong, S. L.; Zhang, H.; Wu, Z.; Tai, G.; Wang, X. X.; Hu, T.; Zheng, W.; Jiang, Y.; Hu, X.; Li, H. H. H.; Zeng, Z.; Wang, X. X.; Mak, K. F.; Shan, J.; Luo, B.; Liu, G.; Wang, L.; Geng, D.; Yang, H. Y.; Choi, W.; Choudhary, N.; Han, G. H.; Park, J.; Akinwande, D.; Lee, Y. H.; Brent, J. R.; Savjani, N.; Brien, P. O. Emerging Energy Applications of Two-Dimensional Layered Transition Metal Dichalcogenides. *Nano Energy* **2015**, *18* (4), 293–305. <https://doi.org/10.1016/j.nanoen.2015.10.023>.
- (11) Luo, B.; Liu, G.; Wang, L. Recent Advances in 2D Materials for Photocatalysis. *Nanoscale* **2016**, *8* (13), 6904–6920. <https://doi.org/10.1039/C6NR00546B>.
- (12) Shim, G. W.; Hong, W.; Yang, S. Y.; Choi, S.-Y. Y. Tuning the Catalytic Functionality of Transition Metal Dichalcogenides Grown by Chemical Vapour Deposition. *J. Mater. Chem.*

- A **2017**, 5 (29), 14950–14968. <https://doi.org/10.1039/C7TA03039H>.
- (13) Noh, S. H.; Hwang, J.; Kang, J.; Seo, M. H.; Choi, D.; Han, B. Tuning the Catalytic Activity of Heterogeneous Two-Dimensional Transition Metal Dichalcogenides for Hydrogen Evolution. *J. Mater. Chem. A* **2018**, 6 (41), 20005–20014. <https://doi.org/10.1039/C8TA07141A>.
- (14) Zou, X.; Zhang, Y. Noble Metal-Free Hydrogen Evolution Catalysts for Water Splitting. *Chem. Soc. Rev.* **2015**, 44 (15), 5148–5180. <https://doi.org/10.1039/C4CS00448E>.
- (15) Yan, Y.; Xia, B. Y.; Zhao, B.; Wang, X. A Review on Noble-Metal-Free Bifunctional Heterogeneous Catalysts for Overall Electrochemical Water Splitting. *J. Mater. Chem. A* **2016**, 4 (45), 17587–17603. <https://doi.org/10.1039/C6TA08075H>.
- (16) Eftekhari, A. Molybdenum Diselenide (MoSe₂) for Energy Storage, Catalysis, and Optoelectronics. *Appl. Mater. Today* **2017**, 8, 1–17. <https://doi.org/10.1016/j.apmt.2017.01.006>.
- (17) Yu, Y.; Nam, G. H.; He, Q.; Wu, X. J.; Zhang, K.; Yang, Z.; Chen, J.; Ma, Q.; Zhao, M.; Liu, Z.; Ran, F. R.; Wang, X.; Li, H.; Huang, X.; Li, B.; Xiong, Q.; Zhang, Q.; Liu, Z.; Gu, L.; Du, Y.; Huang, W.; Zhang, H. High Phase-Purity 1T'-MoS₂ - and 1T'-MoSe₂ -Layered Crystals. *Nat. Chem.* **2018**, 10 (6), 638–643. <https://doi.org/10.1038/s41557-018-0035-6>.
- (18) Ojha, M.; Deepa, M. Molybdenum Selenide Nanotubes Decorated Carbon Net for a High Performance Supercapacitor. *Chem. Eng. J.* **2019**, 368 (February), 772–783. <https://doi.org/10.1016/j.cej.2019.03.002>.
- (19) Mariappan, V. K.; Krishnamoorthy, K.; Pazhamalai, P.; Sahoo, S.; Kim, S. J.

- Electrodeposited Molybdenum Selenide Sheets on Nickel Foam as a Binder-Free Electrode for Supercapacitor Application. *Electrochim. Acta* **2018**, *265*, 514–522. <https://doi.org/10.1016/j.electacta.2018.01.075>.
- (20) Liu, Y.; Zhu, M.; Chen, D. Sheet-like MoSe₂/C Composites with Enhanced Li-Ion Storage Properties. *J. Mater. Chem. A* **2015**, *3* (22), 11857–11862. <https://doi.org/10.1039/C5TA02100F>.
- (21) Yao, J.; Liu, B.; Ozden, S.; Wu, J.; Yang, S.; Rodrigues, M. T. F.; Kalaga, K.; Dong, P.; Xiao, P.; Zhang, Y.; Vajtai, R.; Ajayan, P. M. 3D Nanostructured Molybdenum Diselenide/Graphene Foam as Anodes for Long-Cycle Life Lithium-Ion Batteries. *Electrochim. Acta* **2015**, *176*, 103–111. <https://doi.org/10.1016/j.electacta.2015.06.138>.
- (22) Zhang, Z.; Fu, Y.; Yang, X.; Qu, Y.; Zhang, Z. Hierarchical MoSe₂ Nanosheets/Reduced Graphene Oxide Composites as Anodes for Lithium-Ion and Sodium-Ion Batteries with Enhanced Electrochemical Performance. *ChemNanoMat* **2015**, *1* (6), 409–414. <https://doi.org/10.1002/cnma.201500097>.
- (23) Chang, Y.-H.; Zhang, W.; Zhu, Y.; Han, Y.; Pu, J.; Chang, J.-K.; Hsu, W.-T.; Huang, J.-K.; Hsu, C.-L.; Chiu, M.-H.; Takenobu, T.; Li, H.; Wu, C.-I.; Chang, W.-H.; Wee, A. T. S.; Li, L.-J. Monolayer MoSe₂ Grown by Chemical Vapor Deposition for Fast Photodetection. *ACS Nano* **2014**, *8* (8), 8582–8590. <https://doi.org/10.1021/nn503287m>.
- (24) Silva, J. P. B.; Almeida Marques, C.; Viana, A. S.; Santos, L. F.; Gwozdz, K.; Popko, E.; Connolly, J. P.; Veltruská, K.; Matolín, V.; Conde, O. Morphological, Optical and Photovoltaic Characteristics of MoSe₂/SiO_x/Si Heterojunctions. *Sci. Rep.* **2020**, *10* (1), 1–9. <https://doi.org/10.1038/s41598-020-58164-7>.

- (25) Jung, C.; Kim, S. M.; Moon, H.; Han, G.; Kwon, J.; Hong, Y. K.; Omkaram, I.; Yoon, Y.; Kim, S.; Park, J. Highly Crystalline CVD-Grown Multilayer MoSe₂ Thin Film Transistor for Fast Photodetector. *Sci. Rep.* **2015**, *5*, 1–9. <https://doi.org/10.1038/srep15313>.
- (26) Jha, R. K.; D'Costa, J. V.; Sakhuja, N.; Bhat, N. MoSe₂ Nanoflakes Based Chemiresistive Sensors for Ppb-Level Hydrogen Sulfide Gas Detection. *Sensors Actuators B Chem.* **2019**, *297*, 126687. <https://doi.org/10.1016/j.snb.2019.126687>.
- (27) Jiang, F.; Zhao, W.-S.; Zhang, J. Mini-Review: Recent Progress in the Development of MoSe₂ Based Chemical Sensors and Biosensors. *Microelectron. Eng.* **2020**, *225*, 111279. <https://doi.org/10.1016/j.mee.2020.111279>.
- (28) Tang, H.; Huang, H.; Wang, X.; Wu, K.; Tang, G.; Li, C. Hydrothermal Synthesis of 3D Hierarchical Flower-like MoSe₂ Microspheres and Their Adsorption Performances for Methyl Orange. *Appl. Surf. Sci.* **2016**, *379*, 296–303. <https://doi.org/10.1016/j.apsusc.2016.04.086>.
- (29) Yang, X.; Wu, R.; Liu, H.; Fan, H.; Zhang, H.; Sun, Y. Amorphous Molybdenum Selenide as Highly Efficient Photocatalyst for the Photodegradation of Organic Dyes under Visible Light. *Appl. Surf. Sci.* **2018**, *457* (May), 214–220. <https://doi.org/10.1016/j.apsusc.2018.06.039>.
- (30) Jiang, M.; Zhang, J.; Wu, M.; Jian, W.; Xue, H.; Ng, T. W.; Lee, C. S.; Xu, J. Synthesis of 1T-MoSe₂ Ultrathin Nanosheets with an Expanded Interlayer Spacing of 1.17 Nm for Efficient Hydrogen Evolution Reaction. *J. Mater. Chem. A* **2016**, *4* (39), 14949–14953. <https://doi.org/10.1039/c6ta07020e>.

- (31) Xiao, W.; Bukhvalov, D.; Zou, Z.; Zhang, L.; Lin, Z.; Yang, X. Unveiling the Origin of the High Catalytic Activity of Ultrathin 1T/2H MoSe₂ Nanosheets for the Hydrogen Evolution Reaction: A Combined Experimental and Theoretical Study. *ChemSusChem* **2019**, *12* (22), 5015–5022. <https://doi.org/10.1002/cssc.201902149>.
- (32) Gupta, U.; Naidu, B. S.; Maitra, U.; Singh, A.; Shirodkar, S. N.; Waghmare, U. V.; Rao, C. N. R. Characterization of Few-Layer 1T-MoSe₂ and Its Superior Performance in the Visible-Light Induced Hydrogen Evolution Reaction. *APL Mater.* **2014**, *2* (9), 092802. <https://doi.org/10.1063/1.4892976>.
- (33) Huang, Y.; Lu, H.; Gu, H.; Fu, J.; Mo, S.; Wei, C.; Miao, Y.-E.; Liu, T. A CNT@MoSe₂ Hybrid Catalyst for Efficient and Stable Hydrogen Evolution. *Nanoscale* **2015**, *7* (44), 18595–18602. <https://doi.org/10.1039/C5NR05739F>.
- (34) Qu, B.; Yu, X.; Chen, Y.; Zhu, C.; Li, C.; Yin, Z.; Zhang, X. Ultrathin MoSe₂ Nanosheets Decorated on Carbon Fiber Cloth as Binder-Free and High-Performance Electrocatalyst for Hydrogen Evolution. *ACS Appl. Mater. Interfaces* **2015**, *7* (26), 14170–14175. <https://doi.org/10.1021/acsami.5b02753>.
- (35) Dai, C.; Zhou, Z.; Tian, C.; Li, Y.; Yang, C.; Gao, X.; Tian, X. Large-Scale Synthesis of Graphene-Like MoSe₂ Nanosheets for Efficient Hydrogen Evolution Reaction. *J. Phys. Chem. C* **2017**, *121* (3), 1974–1981. <https://doi.org/10.1021/acs.jpcc.6b11423>.
- (36) Mao, S.; Wen, Z.; Ci, S.; Guo, X.; Ostrikov, K. K.; Chen, J. Perpendicularly Oriented MoSe₂/Graphene Nanosheets as Advanced Electrocatalysts for Hydrogen Evolution. *Small* **2015**, *11* (4), 414–419. <https://doi.org/10.1002/sml.201401598>.

- (37) Barough, V.; Iranizad, E. S.; Bayat, A.; Hemmati, K. Synthesis of Binder-Free MoSe₂ Nanoflakes as a New Electrode for Electrocatalytic Hydrogen Evolution. *J. Electroanal. Chem.* **2018**, *823*, 278–286. <https://doi.org/10.1016/j.jelechem.2018.06.022>.
- (38) Oh, N. K.; Kim, C.; Lee, J.; Kwon, O.; Choi, Y.; Jung, G. Y.; Lim, H. Y.; Kwak, S. K.; Kim, G.; Park, H. In-Situ Local Phase-Transitioned MoSe₂ in La_{0.5}Sr_{0.5}CoO_{3-δ} Heterostructure and Stable Overall Water Electrolysis over 1000 Hours. *Nat. Commun.* **2019**, *10* (1), 1–12. <https://doi.org/10.1038/s41467-019-09339-y>.
- (39) Huang, Y.; Miao, Y.-E.; Fu, J.; Mo, S.; Wei, C.; Liu, T. Perpendicularly Oriented Few-Layer MoSe₂ on SnO₂ Nanotubes for Efficient Hydrogen Evolution Reaction. *J. Mater. Chem. A* **2015**, *3* (31), 16263–16271. <https://doi.org/10.1039/C5TA03704B>.
- (40) Chen, X.; Liu, G.; Zheng, W.; Feng, W.; Cao, W.; Hu, W.; Hu, P. Vertical 2D MoO₂/MoSe₂ Core-Shell Nanosheet Arrays as High-Performance Electrocatalysts for Hydrogen Evolution Reaction. *Adv. Funct. Mater.* **2016**, *26* (46), 8537–8544. <https://doi.org/10.1002/adfm.201603674>.
- (41) Zhang, Y.; Zhu, H.; Yu, L.; He, J.; Huang, C. MoSe₂ Modified TiO₂ Nanotube Arrays with Superior Photoelectrochemical Performance. *Mater. Res. Express* **2018**, *5* (4), 045014. <https://doi.org/10.1088/2053-1591/aab90c>.
- (42) Wu, L.; Shi, S.; Li, Q.; Zhang, X.; Cui, X. TiO₂ Nanoparticles Modified with 2D MoSe₂ for Enhanced Photocatalytic Activity on Hydrogen Evolution. *Int. J. Hydrogen Energy* **2019**, *44* (2), 720–728. <https://doi.org/10.1016/j.ijhydene.2018.10.214>.
- (43) Kong, D.; Wang, H.; Cha, J. J.; Pasta, M.; Koski, K. J.; Yao, J.; Cui, Y. Synthesis of MoS₂

- and MoSe₂ Films with Vertically Aligned Layers. *Nano Lett.* **2013**, *13* (3), 1341–1347.
<https://doi.org/10.1021/nl400258t>.
- (44) Zheng, X.; Yang, L. L.; Li, Y.; Yang, L. L.; Luo, S. Direct Z-Scheme MoSe₂ Decorating TiO₂ Nanotube Arrays Photocatalyst for Water Decontamination. *Electrochim. Acta* **2019**, *298*, 663–669. <https://doi.org/10.1016/j.electacta.2018.12.130>.
- (45) Chu, H.; Liu, X.; Liu, B.; Zhu, G.; Lei, W.; Du, H.; Liu, J.; Li, J.; Li, C.; Sun, C. Hexagonal 2H-MoSe₂ Broad Spectrum Active Photocatalyst for Cr(VI) Reduction. *Sci. Rep.* **2016**, *6* (1), 35304. <https://doi.org/10.1038/srep35304>.
- (46) Hussain, S.; Vikraman, D.; Akbar, K.; Naqvi, B. A.; Abbas, S. M.; Kim, H. S.; Chun, S. H.; Jung, J. Fabrication of MoSe₂ Decorated Three-Dimensional Graphene Composites Structure as a Highly Stable Electrocatalyst for Improved Hydrogen Evolution Reaction. *Renew. Energy* **2019**, *143*, 1659–1669. <https://doi.org/10.1016/j.renene.2019.05.126>.
- (47) Pazhamalai, P.; Krishnamoorthy, K.; Sahoo, S.; Kim, S. J. Two-Dimensional Molybdenum Diselenide Nanosheets as a Novel Electrode Material for Symmetric Supercapacitors Using Organic Electrolyte. *Electrochim. Acta* **2019**, *295*, 591–598. <https://doi.org/10.1016/j.electacta.2018.10.191>.
- (48) Zhang, Z.; Yang, X.; Fu, Y.; Du, K. Ultrathin Molybdenum Diselenide Nanosheets Anchored on Multi-Walled Carbon Nanotubes as Anode Composites for High Performance Sodium-Ion Batteries. *J. Power Sources* **2015**, *296*, 2–9. <https://doi.org/10.1016/j.jpowsour.2015.07.008>.
- (49) Najafi, L.; Bellani, S.; Oropesa-Nuniez, R.; Prato, M.; Martín-García, B.; Brescia, R.;

- Bonaccorso, F. Carbon Nanotube-Supported MoSe₂ Holey Flake:Mo₂C Ball Hybrids for Bifunctional PH-Universal Water Splitting. *ACS Nano* **2019**, *13* (3), 3162–3176. <https://doi.org/10.1021/acsnano.8b08670>.
- (50) Wang, B. B.; Zhu, M. K.; Ostrikov, K.; Shao, R. W.; Zheng, K. Structure and Photoluminescence of Molybdenum Selenide Nanomaterials Grown by Hot Filament Chemical Vapor Deposition. *J. Alloys Compd.* **2015**, *647*, 734–739. <https://doi.org/10.1016/j.jallcom.2015.05.237>.
- (51) Yang, Y.; Huo, N.; Li, J. Gate Modulated and Enhanced Optoelectronic Performance of MoSe₂ and CVD-Grown MoS₂ Heterojunctions. *RSC Adv.* **2017**, *7* (65), 41052–41056. <https://doi.org/10.1039/c7ra07672j>.
- (52) Tsang, C. F.; Ledina, M. A.; Stickney, J. L. Molybdenum Diselenide Formation Using Electrochemical Atomic Layer Deposition (E-ALD). *J. Electroanal. Chem.* **2017**, *793*, 242–249. <https://doi.org/10.1016/j.jelechem.2017.01.065>.
- (53) Krbal, M.; Příkryll, J.; Zazpe, R.; Dvořák, F.; Bureš, F.; Macák, J. M. 2D MoSe₂ Structures Prepared by Atomic Layer Deposition. *Phys. Status Solidi - Rapid Res. Lett.* **2018**, *12* (5), 4–7. <https://doi.org/10.1002/pssr.201800023>.
- (54) Zazpe, R.; Charvot, J.; Krumpolec, R.; Hromádka, L.; Pavliňák, D.; Dvorak, F.; Knotek, P.; Michalicka, J.; Příkryl, J.; Ng, S.; Jelínková, V.; Bureš, F.; Macak, J. M. Atomic Layer Deposition of MoSe₂ Using New Selenium Precursors. *FlatChem* **2020**, *21* (April), 100166. <https://doi.org/10.1016/j.flatc.2020.100166>.
- (55) Charvot, J.; Pokorný, D.; Zazpe, R.; Krumpolec, R.; Pavliňák, D.; Hromádka, L.; Příkryl,

- J.; Rodriguez-Pereira, J.; Klikar, M.; Jelínková, V.; Macak, J. M.; Bureš, F. Cyclic Silylselenides: Convenient Selenium Precursors for Atomic Layer Deposition. *Chempluschem* **2020**, *85* (3), 576–579. <https://doi.org/10.1002/cplu.202000108>.
- (56) Cremers, V.; Puurunen, R. L.; Dendooven, J. Conformality in Atomic Layer Deposition: Current Status Overview of Analysis and Modelling. *Appl. Phys. Rev.* **2019**, *6* (2), 021302. <https://doi.org/10.1063/1.5060967>.
- (57) Detavernier, C.; Dendooven, J.; Sree, S. P.; Ludwig, K. F.; Martens, J. A. Tailoring Nanoporous Materials by Atomic Layer Deposition. *Chem. Soc. Rev.* **2011**, *40* (11), 5242–5253. <https://doi.org/10.1039/c1cs15091j>.
- (58) Dvorak, F.; Zazpe, R.; Krbal, M.; Sopha, H.; Prikryl, J.; Ng, S.; Hromadko, L.; Bures, F.; Macak, J. M. One-Dimensional Anodic TiO₂ Nanotubes Coated by Atomic Layer Deposition: Towards Advanced Applications. *Appl. Mater. Today* **2019**, *14*, 1–20. <https://doi.org/10.1016/j.apmt.2018.11.005>.
- (59) Cai, J.; Han, X.; Wang, X.; Meng, X. Atomic Layer Deposition of Two-Dimensional Layered Materials: Processes, Growth Mechanisms, and Characteristics. *Matter*. 2020. <https://doi.org/10.1016/j.matt.2019.12.026>.
- (60) Ng, S.; Krbal, M.; Zazpe, R.; Prikryl, J.; Charvot, J.; Dvořák, F.; Strizik, L.; Slang, S.; Sopha, H.; Kosto, Y.; Matolin, V.; Yam, F. K.; Bures, F.; Macak, J. M. MoSexOy-Coated 1D TiO₂ Nanotube Layers: Efficient Interface for Light-Driven Applications. *Adv. Mater. Interfaces* **2018**. <https://doi.org/10.1002/admi.201701146>.
- (61) Sopha, H.; Tesfaye, A. T.; Zazpe, R.; Michalicka, J.; Dvorak, F.; Hromadko, L.; Krbal, M.;

- Prikryl, J.; Djenizian, T.; Macak, J. M. ALD Growth of MoS₂ Nanosheets on TiO₂ Nanotube Supports. *FlatChem* **2019**. <https://doi.org/10.1016/j.flatc.2019.100130>.
- (62) Motola, M.; Baudys, M.; Zazpe, R.; Krbal, M.; Michalička, J.; Rodriguez-Pereira, J.; Pavliňák, D.; Prikryl, J.; Hromádko, L.; Sopha, H.; Krýsa, J.; Macak, J. M. 2D MoS₂ Nanosheets on 1D Anodic TiO₂ Nanotube Layers: An Efficient Co-Catalyst for Liquid and Gas Phase Photocatalysis. *Nanoscale* **2019**, *11* (48), 23126–23131. <https://doi.org/10.1039/C9NR08753B>.
- (63) Das, S.; Sopha, H.; Krbal, M.; Zazpe, R.; Podzemna, V.; Prikryl, J.; Macak, J. M. Electrochemical Infilling of CuInSe₂ within TiO₂ Nanotube Layers and Subsequent Photoelectrochemical Studies. *ChemElectroChem* **2017**, *4* (3), 495–499. <https://doi.org/10.1002/celec.201600763>.
- (64) Motola, M.; Hromádko, L.; Prikryl, J.; Sopha, H.; Krbal, M.; Macak, J. M. Intrinsic Properties of High-Aspect Ratio Single- and Double-Wall Anodic TiO₂ Nanotube Layers Annealed at Different Temperatures. *Electrochim. Acta* **2020**, *352*, 136479. <https://doi.org/10.1016/j.electacta.2020.136479>.
- (65) Rodriguez-Pereira, J.; Zazpe, R.; Charvot, J.; Bureš, F.; Macak, J. M. Molybdenum Diselenide Thin Films Grown by Atomic Layer Deposition: An XPS Analysis. *Surf. Sci. Spectra* **2020**, *27* (2), 024006. <https://doi.org/10.1116/6.0000354>.
- (66) Ng, S.; Kuberský, P.; Krbal, M.; Prikryl, J.; Gärtnerová, V.; Moravcová, D.; Sopha, H.; Zazpe, R.; Yam, F. K.; Jäger, A.; Hromádko, L.; Beneš, L.; Hamáček, A.; Macak, J. M. ZnO Coated Anodic 1D TiO₂ Nanotube Layers: Efficient Photo-Electrochemical and Gas Sensing Heterojunction. *Adv. Eng. Mater.* **2018**, *20* (2), 1700589.

<https://doi.org/10.1002/adem.201700589>.

- (67) Zazpe, R.; Sopha, H.; Prikryl, J.; Krbal, M.; Mistrik, J.; Dvorak, F.; Hromadko, L.; Macak, J. M. A 1D Conical Nanotubular TiO₂/CdS Heterostructure with Superior Photon-to-Electron Conversion. *Nanoscale* **2018**, *10*, 16601–16612. <https://doi.org/10.1039/c8nr02418a>.
- (68) Krbal, M.; Ng, S.; Motola, M.; Hromadko, L.; Dvorak, F.; Prokop, V.; Sopha, H.; Macak, J. M. Sulfur Treated 1D Anodic TiO₂ Nanotube Layers for Significant Photo- and Electroactivity Enhancement. *Appl. Mater. Today* **2019**, *17*, 104–111. <https://doi.org/10.1016/j.apmt.2019.07.018>.
- (69) Wu, Y.; Xu, M.; Chen, X.; Yang, S.; Wu, H.; Pan, J.; Xiong, X. CTAB-Assisted Synthesis of Novel Ultrathin MoSe₂ Nanosheets Perpendicular to Graphene for the Adsorption and Photodegradation of Organic Dyes under Visible Light. *Nanoscale* **2016**, *8* (1), 440–450. <https://doi.org/10.1039/c5nr05748e>.
- (70) Valdés, H.; Molina, L. M.; Alonso, J. A. Water Adsorption and Dissociation on Gold Catalysts Supported on Anatase-TiO₂(101). *Appl. Surf. Sci.* **2019**, *487*, 244–252. <https://doi.org/10.1016/j.apsusc.2019.04.249>.

Table of Contents/Abstract Graphic

